Cladded phononic nodal frame state in biatomic alkali-metal sulfides

Tie Yang,[1,2] Yang Gao,[1] Liyu Hao,[1,3] Haopeng Zhang,[4] Xingwen Tan,[1] Peng Wang,[1] Zhenxiang Cheng,[5,*] and Weikang Wu[6,†]

[1]*School of Physical Science and Technology, Southwest University, Chongqing 400715, China*
[2]*College of Physics, Chongqing University, Chongqing 400044, China*
[3]*State Key Laboratory of Nuclear Physics and Technology, Department of Technical Physics, School of Physics, Peking University, Beijing 100871, China*
[4]*School of Science, Chongqing University of Posts and Telecommunications, Chongqing 400065, China*
[5]*Institute for Superconducting and Electronic Materials, University of Wollongong, Wollongong 2500, Australia*
[6]*Key Laboratory for Liquid-Solid Structural Evolution and Processing of Materials, Ministry of Education, Shandong University, Jinan 250061, China*

(Received 4 July 2023; accepted 9 October 2023; published 23 October 2023)

With rapid progress, the current study of topological properties in condensed matter systems has been further extended from the electronic scope to the phononic perspective. Based on first-principles calculations, we present a systematic investigation on topological phononic states in a series of biatomic alkali-metal sulfides AB (A = Na, K; B = S, Se, Te). Taking NaSe as an example, clear topological features of the nodal line and nodal surface states are revealed, and these two states, originating from the same two bands, concatenate together into a cladded nodal frame structure. Detailed symmetry arguments and effective Hamiltonian analysis show that the occurrence of the cladded nodal frame structure is determined by the combination of both symmorphic and nonsymmorphic symmetries. The phonon surface spectrum is calculated on the (010) surface and clean surface states are observed, which not only confirms their nontrivial topological feature, but also benefits their experimental verification. This cladded nodal frame structure can provide an ideal platform to examine the exotic topological phononic states and, with the present material candidates, especially those that have been synthesized, the corresponding experimental studies can be immediately advanced.

DOI: 10.1103/PhysRevB.108.134310

I. INTRODUCTION

Topological ordered states, as intrinsic properties of condensed matters, have attracted extensive scientific attention in the recent solid-state physics community. In particular, the discovery of topological insulators has sparked tremendous research interest in this field [1–5], and intensive effort has been dedicated to the study of diverse topological phases and their corresponding exotic surface properties from both theoretical and experimental perspectives. Years of continuous development have led to the successful establishment of topological band theory [6–10], which has been not only adequately demonstrated from experimental verification, but also effectively applied to searching for new topological materials [11–20]. The theoretical studies have been especially facilitated and, with the combination of high throughput computation methods, several topological material databases have been created, such as the topological materials database [16], the topological materials arsenal [12], materiae [14], the topological magnetic materials database [17,19], and the topological phononics of materials [21,22].

With the rapid progress in this field, the study of topological properties in solid-state systems has been recently extended from the conventional electronic scope to the phononic scale [23–30]. Similar to electrons, phonons, as the other basic emergent particles of the crystalline lattice, also share topological features from crystal symmetry constraints. Two major differences, however, are responsible for the larger advantage of topological phonons than topological electrons; i.e., the phonons as boson particles are not restrained by the Pauli exclusion principle, which can remove the energy limitation from the search for topological states in electronic system and the spin orbital coupling effect can be neglected, which can provide an ideal manner to examine the different topological states [31–34]. According to the band degeneracy, topological charge, and dispersion conditions, topological phononic states can be divided into different types [35]. For instance, the nodal point [36–40], nodal line [41,42], and nodal surface [43–45] phonons can be distinguished according to their band-crossing dimensionality; Weyl [32], triple [46], Dirac [47–49], and sixfold topological phonon [50] elements can be differentiated by their band degeneracy; and the linear, quadratic, and cubic topological phonon states can be discriminated from their band dispersion order [51,52]. In addition, some other topological phonon structures can be categorized based on their band-crossing distribution or their interwining shape, e.g., the nodal link [53], nodal net [54], nodal chain [55,56], and nodal cage phonon [57].

Like their electronic counterparts, the topological phononic states are also associated with nontrivial surface states, such as

*cheng@uow.edu.au
†weikang_wu@sdu.edu.cn

surface arc and drumhead states for nodal points and nodal lines. Indeed, these exotic surface states are the ultimate topological aspects, especially for the purposes of potential application. Compared with the enormous studies on topological electronic states, the corresponding research on phonons is still rare, and there is still a great scarcity of ideal material candidates. Under these circumstances, we present a systematic first-principles investigation on a series of biatomic alkali-metal sulfides AB (A = Na, K; B = S, Se, Te). Their phonon bands exhibit ideal topological features of the nodal line and nodal surface states. More importantly, these two states originate from the same two bands, and they together form a cladded nodal frame structure. Detailed symmetry analysis and effective Hamiltonian deliberation revealed that the concurrence of this cladded nodal frame structure is determined by both symmorphic and nonsymmorphic symmetries. Calculated surface states further confirm their nontrivial topological features. Compared with previous studies, the current material family and the identified cladded nodal frame state cannot only serve as an ideal platform to examine the corresponding topological phononic states, but also provide an effective approach to investigate the possible correlation effects between the nodal line and nodal surface states. Since some of the presented materials have been synthesized, their experimental investigation can be immediately inspired.

II. COMPUTATIONAL METHODOLOGY

In the current study, on the basis of first-principles calculations, we studied the alkali-metal sulfide compounds AB (A = Na, K; B = S, Se, Te) by using the Vienna *ab initio* simulation package (VASP) [58] under the framework of density function theory (DFT) [59]. The projector augmented wave (PAW) method [60] was applied for the interactions between ions and valence electrons, and the generalized gradient approximation (GGA) of the revised Perdew-Burke-Ernzerhof (PBEsol) formalism [61,62] was employed for the exchange correlation functional. The cutoff energy for the plane wave set was selected as 520 eV, and a Γ centered k mesh of $5 \times 5 \times 6$ was set to sample the first Brillouin zone. The ground-state structure was fully relaxed until the total force was smaller than 1×10^{-4} eV/Å per atom and the self-consistent loop was reached when the total energy variation per atom was smaller than 1×10^{-6} eV. To study the topological properties, the PHONOPY program [63] was utilized to calculate the force constant with the density functional perturbation theory [64,65], and based on this, a Wannier tight-binding Hamiltonian was constructed for examination of the topological surface characteristics by the WANNIERTOOLS package [66].

III. RESULTS AND DISCUSSIONS

The binary alkali-metal sulfides AB (A = Na, K; B = S, Se, Te) have the hexagonal crystal structure (space group $P63/mmc$, No. 194), and they are screened out from high throughput calculations. Among them, three members have been experimentally synthesized [67,68], including NaS, NaSe, and KTe. Taking NaSe as an example, the corresponding unit cell is shown in Fig. 1(a), and it includes four Na atoms located at the $2a$ (0, 0, 0) and $2c$ (1/3, 2/3, 1/4)

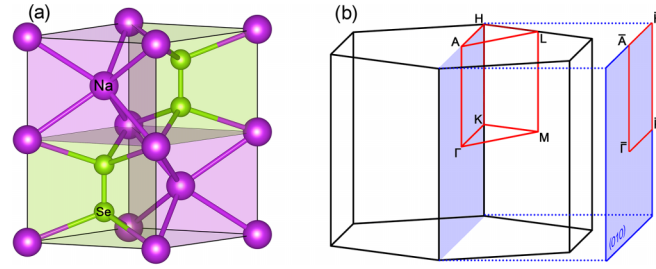

FIG. 1. The unit cell (a) of NaSe compound with the hexagonal crystal structure and the corresponding first Brillouin zone (b) with high symmetry paths and points labeled. The translucent area on the right side indicates the (010) surface projection.

Wyckoff sites and four Se atoms located at the $4f(1/3, 2/3, z)$ Wyckoff sites, where z is the local coordination. As displayed by the different color-shaded areas in the figure, the bonding between Na and Se atoms forms four polyhedra in which a single Na atom or a pair of Se atoms are alternately situated at the center and Na atoms are distributed at the six corners. From the fully relaxed crystal structure, the lattice constants are obtained, $a = b = 4.695$ Å, $c = 10.774$ Å, and $z = 0.63524$, which are in very good agreement with the experimental values, $a = b = 4.726$ Å, $c = 10.788$ Å, and $z = 0.63527$, with deviation less than 1%. Therefore, this optimized crystal lattice will be used for the following calculations and discussions. The calculated and experimental lattice constants of the other compounds are provided in the Supplemental Material [69].

Based on the relaxed crystal structures, we first calculated the phononic band structure, and the results for NaSe are reported in Fig. 2. The high symmetry points and paths were selected by the SeeK-path tool [70], and their corresponding

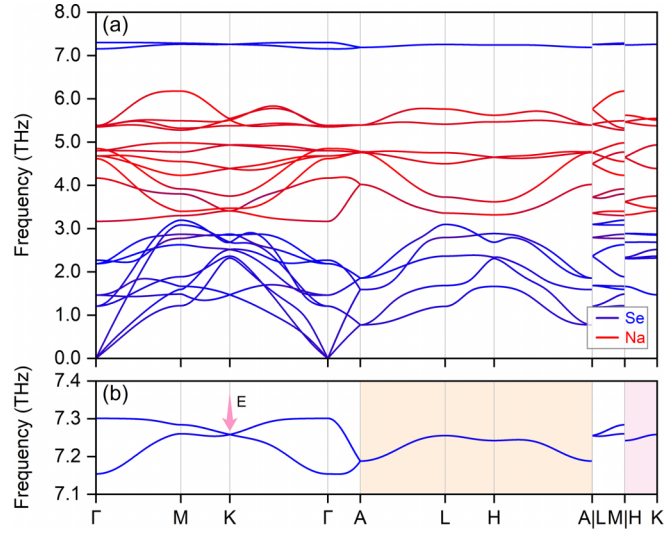

FIG. 2. The calculated phononic band structures (a) with element contribution projected by the different color weights for NaSe compound. Enlargement of the local crossing bands (b) for phononic topological study. The band crossing point and double degeneracy are indicated by the red arrow and color-shaded area. The irreducible representation of the degenerate band along H-K is E.

locations in the Brillouin zone are shown in Fig. 1(b). For the other materials, their calculated phonon bands are shown in the Supplemental Material [69]. From these phononic bands, we can see that they do not exhibit any imaginary frequency or soft phonon mode, which indicates their dynamic stability at low temperature and also reflects the possible experimental synthesis for three theoretical materials. Taking NaSe as an example, it is interestingly found that the phononic bands can be separated into three parts with different frequency ranges, and at low frequency the acoustic branches are mixed with the optical branches. In addition, we further projected the element contribution on the phononic band structure with different color weights: blue for Se element and red for Na element. It can be seen that the phononic bands in the frequency range of 0–3 THz and >6 THz are mainly contributed by the Se element, while the other bands at 3–6 THz are from Na element. The highest part is well separated from the other two with a gap of about 1 THz to the middle part. It is composed of only two bands with no other band interference, and its local enlargement is shown in Fig. 2(b), from which we can observe that the two bands form a crossing point at the K point and become completely doubly degenerate along the two paths A-L-H-A and H-K, as indicated by the red arrow and color shaded area. Since the K point is also located along the H-K path, the crossing point at K should actually belong to the doubly degenerate band along the H-K path. Even though the entire frequency range can be accessed for the topological phonon states, we still focus on the top two bands due to the clean band structure and simple crossing condition. In the following, we divide the topological investigation of these top two bands into two regions along the two paths H-K and A-L-H-A, respectively. For the other compounds, the same condition can be applied to the top two bands.

First, the doubly degenerate band along the H-K path is examined. This path is distributed along the vertical border of the hexagonal Brillouin zone, see Fig. 1(b), and it is perpendicular to the horizontal paths M-K and K-Γ. Considering the band crossing at the K point along the M-K-Γ path, the double degeneracy of this H-K path is formed by the linear crossing of the same two bands from the horizontal direction, and it indeed corresponds to a topological nodal line. To better understand its formation mechanism, we performed a precise dispersion scan of the same two bands along the $k_x = 0$ plane, and the obtained three-dimensional band dispersion is displayed in Fig. 3(a). The corresponding high-symmetry paths and points are shown at the bottom. It can be clearly seen that the two bands cross only along the four rectangular borders and that they are separated elsewhere. Their overlaps at the four borders are highlight by two different colored dots: magenta for the two lines along the H-A direction and red for the other two lines along the H-K direction. From this band dispersion, we confirm that the doubly degenerate nodal line along the H-K path is formed by the linear crossing of the same two bands from the perpendicular plane. In addition, this nodal line stretches through the whole Brillouin zone along the H-K-H′ path, and based on the rotation symmetry, there should be six nodal lines in total, which are symmetrically identical, and they are all located along the vertical border of the hexagonal Brillouin zone. To further confirm the nontrivial band topology of these nodal lines, we calculated

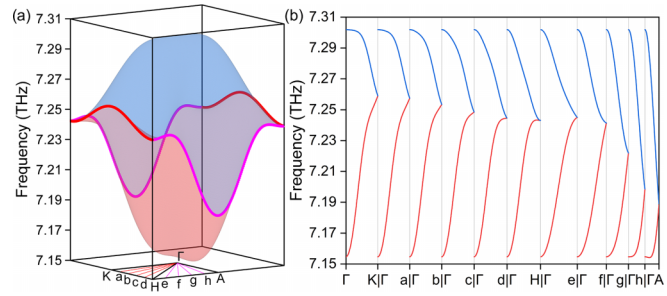

FIG. 3. The three-dimensional phononic band dispersion (a) for NaSe compound in the $k_x = 0$ plane. The band crossing points at the rectangular border are highlighted with red and magenta lines and the coordinate system are shown on the bottom. The local band structures (b) along different path segments for the same two bands.

the phonon Berry phase γ around them by $\gamma = \oint_L A(\mathbf{q}) \cdot d\mathbf{q}$, where $A(\mathbf{q}) = i \sum_m \langle \varphi_m(\mathbf{q}) | \nabla_{\mathbf{q}} | \varphi_m(\mathbf{q}) \rangle$ is the phonon Berry connection, $\varphi_m(\mathbf{q})$ is the phonon Bloch wave function, and L represents a closed circle around the nodal lines. It is found that the Berry phases are either $+\pi$ or $-\pi$ as the closed loop encircles the nodal lines, implying their nontrivial signature. This type of straight nodal line distributed through the whole Brillouin zone is very rare and it is only found in another phononic system with a similar crystal structure [71]. The frequency variation of this straight nodal line is very small, and to have a clear visualization, we additionally perform band scans along several different path segments, which are evenly distributed between H-K and H-A, as shown in the bottom coordinate system of Fig. 3(a). The calculated band structures along these path segments are presented in Fig. 3(b) and the same colors as for the band dispersion in Fig. 3(a) are used. We can find that the crossing points are all located at the path segment ending points, which correspond to the rectangular k border, and the frequency variation of the crossing points along the H-K path is very small, 0.01 THz, compared with that along the H-A path, 0.07 THz.

Second, we focus on the other doubly degenerate band along the A-L-H-A path. Since this path is entirely located within the $k_z = \pi$ plane, we then calculated the full band scan for these two bands. The obtained three-dimensional band dispersion in the $k_z = \pi$ plane is shown in Fig. 4(a). For comparison, we also computed the band variation of the same two bands in the $k_z = 0.9\pi$ plane and plot it in Fig. 4(b). It can be seen that the two bands, which are separated in the $k_z = 0.9\pi$ plane, become a completely doubly degenerate single band in the $k_z = \pi$ plane. Indeed, this double degeneracy corresponds to a nodal surface. In fact, all the bands in the $k_z = \pi$ plane are constrained into double degeneracy, resulting into the nodal surface formation. Note that the two bands in the $k_z = 0.9\pi$ plane shrink into doubly degenerate points at the six corners, which actually belong to the straight nodal line states at the vertical borders in the hexagonal Brillouin zone, as discussed above. Given the small range in the vertical axis, the current nodal surface also has very small frequency variation, 0.07 THz, the same as that along the H-A path.

In previous investigations, either nodal line phonons or nodal surface phonons have been studied. However, they are mostly examined in a discrete manner and there is scarcely

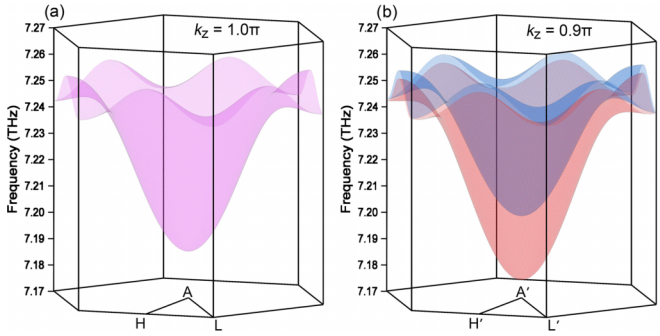

FIG. 4. The three-dimensional phononic band dispersions for NaSe compound in the (a) $k_z = 1.0\pi$ plane and (b) the $k_z = 0.9\pi$ plane. The coordinate system is shown on the bottom for each figure. The purple colored surface in the $k_z = 1.0\pi$ plane is merged from the two bands with red and blue colors, which are separate in the $k_z = 0.9\pi$ plane.

any combination of these two states together in a single platform. Even though the coexistence of nodal lines and nodal surfaces has been revealed in some studies [72,73], different phonon bands have been selected for the two topological states, or the different topological states formed by the same bands are not directly connected. For the current material system, these two nodal phonon states are formed by the same band branches, i.e., the nodal line phonon in the vertical direction, see Fig. 5(a), and the nodal surface phonon in the horizontal direction, see Fig. 5(b). Constituted by the homologous two bands, they join together and result into an exotic cladded nodal frame structure, as shown in Fig. 5(c). Note that this cladded nodal frame phonon defined in the current work differs from the nodal cage or nodal link phonons in other works [53,54,57], which is composed of only nodal lines intersecting or interconnecting from different planes. This unique topological nodal frame state has not been previously reported, and it can offer a special opportunity to analyze the possible correlation effects between the nodal line and surface states. Besides, these two phonon branches that constitute the frame structure are well separated from the rest of the bands and their determined topological states are only located along the high symmetry paths and surfaces without other interference, which can be highly beneficial for the corresponding experimental characterization.

We present the symmetry analysis for the cladded nodal frame structure. The important symmetries include the threefold rotation C_{3z}, the space-time inversion $\mathcal{PT}$, and the combined antiunitary $\tilde{C}_{2z}\mathcal{T}$ symmetries, where $\tilde{C}_{2z} = \{C_{2z}|00\frac{1}{2}\}$ is

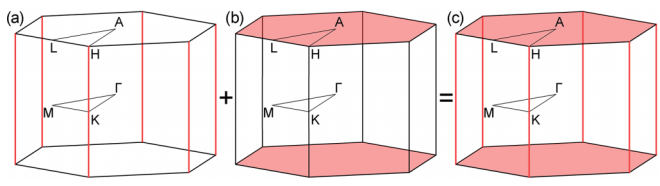

FIG. 5. Illustrations of (a) the nodal line, (b) nodal surface, (c) and cladded nodal frame, as highlighted by the red color structure in the Brillouin zone. The combination of nodal line and nodal surface leads to the formation of the cladded nodal frame structure.

the twofold screw axis along the $\hat{z}$ direction. This cladded nodal frame structure consists of two parts: the nodal surface on the $k_z = \pi$ plane and the nodal lines along the H-K path. The nodal surface is protected by $\tilde{C}_{2z}\mathcal{T}$ since $(\tilde{C}_{2z}\mathcal{T})^2 = -1$ on the $k_z = \pi$ plane, which guarantees the Kramers degeneracy. The nodal line is dictated by C_{3z} and $\mathcal{PT}$, which satisfies the following algebra:

$$C_{3z}^3 = 1, \quad [C_{3z}, \mathcal{PT}] = 0. \tag{1}$$

Since $[C_{3z}, \mathcal{H}(\mathbf{k})] = 0$ along H-K, the Bloch state can be chosen as the eigenstate of C_{3z}, which we denote it as $|c\rangle$, with c being the C_{3z} eigenvalues 1, $e^{\pm i\frac{2\pi}{3}}$. If $\mathcal{PT}$ is represented by complex conjugation, the states $|e^{i\frac{2\pi}{3}}\rangle$ and $|e^{-i\frac{2\pi}{3}}\rangle$ must be degenerate by $\mathcal{PT}$. Away from H-K, C_{3z} is broken and the degenerate states would be violated. Thus, the two states $|e^{i\frac{2\pi}{3}}\rangle$ and $|e^{-i\frac{2\pi}{3}}\rangle$ form a nodal line along H-K. To characterized this nodal line, we construct the $k \cdot p$ effective model in the basis of $\{|e^{i\frac{2\pi}{3}}\rangle, |e^{-i\frac{2\pi}{3}}\rangle\}$. The matrix representations of the generators can be expressed as

$$C_{3z} = e^{i\frac{2\pi}{3}\sigma_z}, \quad \tilde{M}_y = \sigma_x, \quad \mathcal{PT} = \sigma_x\mathcal{K}, \tag{2}$$

in which $\tilde{M}_y = \{M_y|00\frac{1}{2}\}$ is the glide mirror perpendicular to $\hat{y}$ direction, $\mathcal{K}$ is the complex conjugation, $\sigma_i (i = x, y, z)$ are the Pauli matrices. Constrained by the following symmetry requirements

$$\begin{aligned} C_{3z}\mathcal{H}_{\mathtt{eff}}(\mathbf{k})C_{3z}^{-1} &= \mathcal{H}_{\mathtt{eff}}(R_{3z}\mathbf{k}), \\ \tilde{M}_y\mathcal{H}_{\mathtt{eff}}(\mathbf{k})\tilde{M}_y^{-1} &= \mathcal{H}_{\mathtt{eff}}(k_x, -k_y, k_z), \\ (\mathcal{PT})\mathcal{H}_{\mathtt{eff}}(\mathbf{k})(\mathcal{PT})^{-1} &= \mathcal{H}_{\mathtt{eff}}(\mathbf{k}), \end{aligned} \tag{3}$$

with R_{3z} being the rotation acting on $\mathbf{k}$, the Hamiltonian $\mathcal{H}_{\mathtt{eff}}^{\mathtt{H-K}}$ expanded up to the first order is given as

$$\mathcal{H}_{\mathtt{eff}}^{\mathtt{H-K}}(\mathbf{k}) = \upsilon_z k_z\sigma_0 + c(k_x\sigma_x + k_y\sigma_y), \tag{4}$$

where $\mathbf{k}$ is measured from a generic point on the nodal lines, υ_z and c are real parameters, and σ_0 is the 2×2 identity matrix. This effective model confirms the existence of the nodal line along H-K path. At the H point, which is located on the $k_z = \pi$ plane, it is found that the states $|e^{i\frac{2\pi}{3}}\rangle$ and $|e^{-i\frac{2\pi}{3}}\rangle$ form the Kramers pair ensured by $\tilde{C}_{2z}\mathcal{T}$, considering $[C_{3z}, \tilde{C}_{2z}\mathcal{T}] = 0$ and $(\tilde{C}_{2z}\mathcal{T})^2 = -1$. Under the basis of $\{|e^{i\frac{2\pi}{3}}\rangle, |e^{-i\frac{2\pi}{3}}\rangle\}$, $\tilde{C}_{2z}\mathcal{T}$ can be represented as $-i\sigma_y\mathcal{K}$, and the effective Hamiltonian becomes (up to the second order)

$$\mathcal{H}_{\mathtt{eff}}^{\mathtt{H}}(\mathbf{k}) = \epsilon(\mathbf{k}) + c_1k_z(k_x\sigma_x + k_y\sigma_y), \tag{5}$$

where $\epsilon(\mathbf{k}) = \omega_1(k_x^2 + k_y^2) + \omega_2k_z^2$, and $\mathbf{k}$ is measured from a degenerate point at H. This explains the intersection between the nodal line and the nodal surface, which together form the cladded nodal frame structure.

Generally, topological nodal states are intrinsically characterized by their nontrivial surface state and this feature has also been successfully verified for the topological phononic state from both experimental and theoretical perspectives. By constructing a Wannier tight-binding Hamiltonian, we calculated the surface states of these phononic nodal lines through the surface Green's function of a semi-infinite system, which is cleaved along the (010) surface. The slab system has two

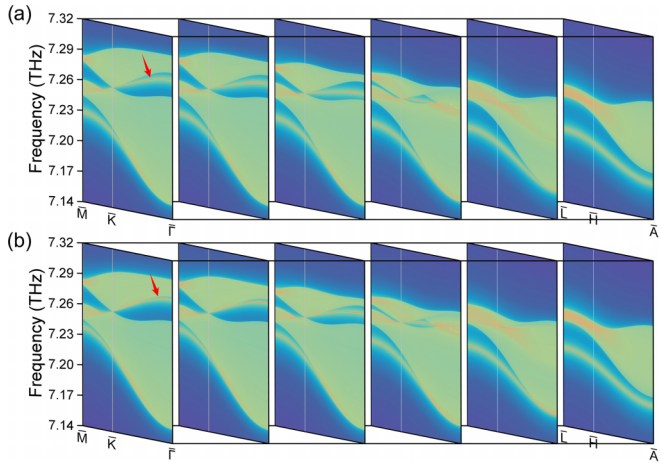

FIG. 6. The calculated surface spectrum along the (010) surface for the (a) top and (b) bottom surfaces, respectively. The drumhead surface states are indicated by the red arrows. The asymmetric surface state distribution is introduced by the dipolar surface terminations.

different types of termination surfaces and this leads to different topological surface states, which has been demonstrated by the asymmetric surface spectra in Figs. 6(a) and 6(b). Since these nodal lines extend straight through the whole Brillouin zone boundary, we have calculated the surface spectra along several path segments, which have a parallel distribution between $\bar{M}$-$\bar{K}$-$\bar{\Gamma}$ and $\bar{L}$-$\bar{H}$-$\bar{A}$. Clear drumhead surface states can be observed, and they have all originated from the band crossing point on the nodal line along $\bar{H}$-$\bar{K}$, as indicated by the red arrows in the figure. Especially for the top surface in Fig. 6(a), the surface states along the different path segments are all well separated from the bulk bands. For the $\bar{L}$-$\bar{H}$-$\bar{A}$ path, the surface spectrum is covered by the bulk band projection since the border point $\bar{H}$ on the nodal line along $\bar{H}$-$\bar{K}$ is coincident with the nodal surface. Considering the other isostructural alkali-metal sulfides and their similar phonon bands, particularly for the same cladded topological nodal frame states formed by the top two bands, the current materials exhibit multiple advantages compared with previous work [34], such as clean band structures, simple band crossing conditions, no other band interference, and evident surface states, and they can be extremely advantageous for future experimental observation and potential application.

IV. CONCLUSION

In the current study, we present a systematic investigation of the phononic topological properties for the alkali-metal sulfide family AB (A = Na, K; B = S, Se, Te) with the help of first-principles calculations. Clear topological band crossing features are revealed by the top two branches of the calculated phononic band spectrum, and they correspond to a nodal line along H-K and a nodal surface in the $k_z = \pi$ plane. Taking NaSe as an example, detailed symmetry analysis and the band formation mechanism are provided, which demonstrates their symmetry-determined protection. The surface properties are calculated based on the Wannier tight-binding Hamiltonian, and clean surface states are observed for both termination surfaces along (010) planes, further confirming the topologically nontrivial feature. Compared with previous studies, the topological nodal line and surface elements are constituted by the homologous two bands, and they join together to form a cladded nodal frame structure. In combination with other isostructural compounds and similar phonon band structures, this material family can thus serve as an ideal platform to examine the corresponding topological phononic states, especially for the study of possible correlation effects between nodal line and nodal surface states.

ACKNOWLEDGMENTS

This work is supported by the National Natural Science Foundation of China (Grants No. 12004315 and No. 11847301), the Natural Science Foundation of Chongqing (Grant No. cstc2021jcyj-msxmX0376) and the Fundamental Research Funds for the Central Universities under Grant No. 2019CDJDWL0005. Z.X. Cheng thanks the Australian Research Council for support (Grant No. DP210101436). W.K. Wu acknowledges the Special Funding in the Project of Qilu Young Scholar Program of Shandong University. The authors thank Dr. Tania Silver for polishing the English of this paper.

[1] M. Z. Hasan and C. L. Kane, Colloquium: Topological insulators, Rev. Mod. Phys. **82**, 3045 (2010).
[2] L. Fu and C. L. Kane, Topological insulators with inversion symmetry, Phys. Rev. B **76**, 045302 (2007).
[3] L. Fu, C. L. Kane, and E. J. Mele, Topological insulators in three dimensions, Phys. Rev. Lett. **98**, 106803 (2007).
[4] A. P. Schnyder, S. Ryu, A. Furusaki, and A. W. W. Ludwig, Classification of topological insulators and superconductors in three spatial dimensions, Phys. Rev. B **78**, 195125 (2008).
[5] X.-L. Qi and S.-C. Zhang, Topological insulators and superconductors, Rev. Mod. Phys. **83**, 1057 (2011).
[6] C.-K. Chiu, J. C. Y. Teo, A. P. Schnyder, and S. Ryu, Classification of topological quantum matter with symmetries, Rev. Mod. Phys. **88**, 035005 (2016).
[7] A. Bansil, H. Lin, and T. Das, Colloquium: Topological band theory, Rev. Mod. Phys. **88**, 021004 (2016).
[8] B. Bradlyn, L. Elcoro, J. Cano, M. G. Vergniory, Z. Wang, C. Felser, M. I. Aroyo, and B. A. Bernevig, Topological quantum chemistry, Nature (London) **547**, 298 (2017).
[9] T. Senthil, Symmetry-protected topological phases of quantum matter, Annu. Rev. Condens. Matter Phys. **6**, 299 (2015).
[10] L. M. Schoop, F. Pielnhofer, and B. V. Lotsch, Chemical principles of topological semimetals, Chem. Mater. **30**, 3155 (2018).
[11] J. Xiao and B. Yan, First-principles calculations for topological quantum materials, Nat. Rev. Phys. **3**, 283 (2021).
[12] F. Tang, H. C. Po, A. Vishwanath, and X. Wan, Efficient topological materials discovery using symmetry indicators, Nat. Phys. **15**, 470 (2019).

[13] P. Narang, C. A. C. Garcia, and C. Felser, The topology of electronic band structures, Nat. Mater. **20**, 293 (2021).
[14] T. Zhang, Y. Jiang, Z. Song, H. Huang, Y. He, Z. Fang, H. Weng, and C. Fang, Catalogue of topological electronic materials, Nature (London) **566**, 475 (2019).
[15] M. G. Vergniory, L. Elcoro, C. Felser, N. Regnault, B. A. Bernevig, and Z. Wang, A complete catalogue of high-quality topological materials, Nature (London) **566**, 480 (2019).
[16] F. Tang, H. C. Po, A. Vishwanath, and X. Wan, Comprehensive search for topological materials using symmetry indicators, Nature (London) **566**, 486 (2019).
[17] L. Elcoro, B. J. Wieder, Z. Song, Y. Xu, B. Bradlyn, and B. A. Bernevig, Magnetic topological quantum chemistry, Nat. Commun. **12**, 5965 (2021).
[18] M. G. Vergniory, B. J. Wieder, L. Elcoro, S. S. P. Parkin, C. Felser, B. A. Bernevig, and N. Regnault, All topological bands of all nonmagnetic stoichiometric materials, Science **376**, eabg9094 (2022).
[19] Y. Xu, L. Elcoro, Z.-D. Song, B. J. Wieder, M. G. Vergniory, N. Regnault, Y. Chen, C. Felser, and B. A. Bernevig, High-throughput calculations of magnetic topological materials, Nature (London) **586**, 702 (2020).
[20] H. Gao, J. W. Venderbos, Y. Kim, and A. M. Rappe, Topological semimetals from first principles, Annu. Rev. Mater. Res. **49**, 153 (2019).
[21] J. Li, J. Liu, S. A. Baronett, M. Liu, L. Wang, R. Li, Y. Chen, D. Li, Q. Zhu, and X.-Q. Chen, Computation and data driven discovery of topological phononic materials, Nat. Commun. **12**, 1204 (2021).
[22] X.-Q. Chen, J. Liu, and J. Li, Topological phononic materials: Computation and data, Innovation **2**, 100134 (2021).
[23] S. H. Mousavi, A. B. Khanikaev, and Z. Wang, Topologically protected elastic waves in phononic metamaterials, Nat. Commun. **6**, 8682 (2015).
[24] R. Süsstrunk and S. D. Huber, Observation of phononic helical edge states in a mechanical topological insulator, Science **349**, 47 (2015).
[25] P. Wang, L. Lu, and K. Bertoldi, Topological phononic crystals with one-way elastic edge waves, Phys. Rev. Lett. **115**, 104302 (2015).
[26] O. Stenull, C. L. Kane, and T. C. Lubensky, Topological phonons and weyl lines in three dimensions, Phys. Rev. Lett. **117**, 068001 (2016).
[27] G. Ding, C. Xie, J. Bai, Z. Cheng, X. Wang, and W. Wu, Recipe for single-pair-Weyl-points phonons carrying the same chiral charges, Phys. Rev. B **108**, L020302 (2023).
[28] Y. Liu, Y. Xu, and W. Duan, Berry phase and topological effects of phonons, Natl. Sci. Rev. **5**, 314 (2018).
[29] B. Peng, Y. Hu, S. Murakami, T. Zhang, and B. Monserrat, Topological phonons in oxide perovskites controlled by light, Sci. Adv. **6**, eabd1618 (2020).
[30] Y. Liu, X. Chen, and Y. Xu, Topological phononics: From fundamental models to real materials, Adv. Funct. Mater. **30**, 1904784 (2020).
[31] Y. Liu, Y. Xu, S.-C. Zhang, and W. Duan, Model for topological phononics and phonon diode, Phys. Rev. B **96**, 064106 (2017).
[32] Q. Xie, J. Li, S. Ullah, R. Li, L. Wang, D. Li, Y. Li, S. Yunoki, and X.-Q. Chen, Phononic Weyl points and one-way topologically protected nontrivial phononic surface arc states in noncentrosymmetric WC-type materials, Phys. Rev. B **99**, 174306 (2019).
[33] F. Zhou, H. Chen, Z.-M. Yu, Z. Zhang, and X. Wang, Realistic cesium fluogermanate: An ideal platform to realize the topologically nodal-box and nodal-chain phonons, Phys. Rev. B **104**, 214310 (2021).
[34] Q.-B. Liu, Z.-Q. Wang, and H.-H. Fu, Topological phonons in allotropes of carbon, Mater. Today Phys. **24**, 100694 (2022).
[35] Z. Yu, Z. Zhang, G.-B. Liu, W. Wu, X.-P. Li, R.-W. Zhang, S. Yang, and Y. Yao, Encyclopedia of emergent particles in three-dimensional crystals, Sci. Bull. **67**, 375 (2022).
[36] Q.-B. Liu, Y. Qian, H.-H. Fu, and Z. Wang, Symmetry-enforced Weyl phonons, npj Comput. Mater. **6**, 95 (2020).
[37] J. Li, L. Wang, J. Liu, R. Li, Z. Zhang, and X.-Q. Chen, Topological phonons in graphene, Phys. Rev. B **101**, 081403(R) (2020).
[38] J. Li, Q. Xie, S. Ullah, R. Li, H. Ma, D. Li, Y. Li, and X.-Q. Chen, Coexistent three-component and two-component weyl phonons in TiS, ZrSe, and HfTe, Phys. Rev. B **97**, 054305 (2018).
[39] W.-W. Yu, Y. Liu, W. Meng, H. Liu, J. Gao, X. Zhang, and G. Liu, Phononic higher-order nodal point in two dimensions, Phys. Rev. B **105**, 035429 (2022).
[40] W.-W. Yu, Y. Liu, X. Zhang, and G. Liu, Topological charge-2 Dirac phonons in three dimensions: Theory and realization, Phys. Rev. B **106**, 195142 (2022).
[41] J. Wang, H. Yuan, Y. Liu, F. Zhou, X. Wang, and G. Zhang, Hourglass Weyl and Dirac nodal line phonons, and drumhead-like and torus phonon surface states in orthorhombic-type KCuS, Phys. Chem. Chem. Phys. **24**, 2752 (2022).
[42] Y. Yang, J. Wang, Y. Liu, Y. Cui, G. Ding, and X. Wang, Topological phonons in Cs-Te binary systems, Phys. Rev. B **107**, 024304 (2023).
[43] Q.-B. Liu, Z.-Q. Wang, and H.-H. Fu, Ideal topological nodal-surface phonons in RbTeAu-family materials, Phys. Rev. B **104**, L041405 (2021).
[44] C. Xie, H. Yuan, Y. Liu, and X. Wang, Two-nodal surface phonons in solid-state materials, Phys. Rev. B **105**, 054307 (2022).
[45] C. Xie, H. Yuan, Y. Liu, X. Wang, and G. Zhang, Three-nodal surface phonons in solid-state materials: Theory and material realization, Phys. Rev. B **104**, 134303 (2021).
[46] S. Singh, Q. S. Wu, C. Yue, A. H. Romero, and A. A. Soluyanov, Topological phonons and thermoelectricity in triple-point metals, Phys. Rev. Mater. **2**, 114204 (2018).
[47] Y. Jin, R. Wang, and H. Xu, Recipe for Dirac phonon states with a quantized valley Berry phase in two-dimensional hexagonal lattices, Nano Lett. **18**, 7755 (2018).
[48] Z. J. Chen, R. Wang, B. W. Xia, B. B. Zheng, Y. J. Jin, Y.-J. Zhao, and H. Xu, Three-dimensional Dirac phonons with inversion symmetry, Phys. Rev. Lett. **126**, 185301 (2021).
[49] J. Wang, H. Yuan, Z.-M. Yu, Z. Zhang, and X. Wang, Coexistence of symmetry-enforced phononic Dirac nodal-line net and three-nodal surfaces phonons in solid-state materials: Theory and materials realization, Phys. Rev. Mater. **5**, 124203 (2021).
[50] C. Xie, Y. Liu, Z. Zhang, F. Zhou, T. Yang, M. Kuang, X. Wang, and G. Zhang, Sixfold degenerate nodal-point phonons: Symmetry analysis and materials realization, Phys. Rev. B **104**, 045148 (2021).

[51] T. Yang, C. Xie, H. Chen, X. Wang, and G. Zhang, Phononic nodal points with quadratic dispersion and multifold degeneracy in the cubic compound Ta_3Sn, Phys. Rev. B **105**, 094310 (2022).

[52] T. Zhang, R. Takahashi, C. Fang, and S. Murakami, Twofold quadruple Weyl nodes in chiral cubic crystals, Phys. Rev. B **102**, 125148 (2020).

[53] Q.-B. Liu, H.-H. Fu, and R. Wu, Topological phononic nodal hexahedron net and nodal links in the high-pressure phase of the semiconductor CuCl, Phys. Rev. B **104**, 045409 (2021).

[54] G. Ding, T. Sun, and X. Wang, Ideal nodal-net, nodal-chain, and nodal-cage phonons in some realistic materials, Phys. Chem. Chem. Phys. **24**, 11175 (2022).

[55] J. Zhu, W. Wu, J. Zhao, H. Chen, L. Zhang, and S. A. Yang, Symmetry-enforced nodal chain phonons, npj Quantum Mater. **7**, 52 (2022).

[56] Y. S. Chen, F. F. Huang, P. Zhou, Z. S. Ma, and L. Z. Sun, Ideal topological phononic nodal chain in K_2O materials class, New J. Phys. **23**, 103043 (2021).

[57] B. Zheng, F. Zhan, X. Wu, R. Wang, and J. Fan, Hourglass phonons jointly protected by symmorphic and nonsymmorphic symmetries, Phys. Rev. B **104**, L060301 (2021).

[58] J. Hafner, *Ab-initio* simulations of materials using VASP: Density-functional theory and beyond, J. Comput. Chem. **29**, 2044 (2008).

[59] M. C. Payne, M. P. Teter, D. C. Allan, T. A. Arias, and J. D. Joannopoulos, Iterative minimization techniques for *ab initio* total-energy calculations: molecular dynamics and conjugate gradients, Rev. Mod. Phys. **64**, 1045 (1992).

[60] P. E. Blochl, Projector augmented-wave method, Phys. Rev. B **50**, 17953 (1994).

[61] J. P. Perdew, K. Burke, and M. Ernzerhof, Generalized gradient approximation made simple, Phys. Rev. Lett. **77**, 3865 (1996).

[62] J. P. Perdew, A. Ruzsinszky, G. I. Csonka, O. A. Vydrov, G. E. Scuseria, L. A. Constantin, X. Zhou, and K. Burke, Restoring the density-gradient expansion for exchange in solids and surfaces, Phys. Rev. Lett. **100**, 136406 (2008).

[63] A. Togo and I. Tanaka, First principles phonon calculations in materials science, Scr. Mater. **108**, 1 (2015).

[64] X. Gonze and C. Lee, Dynamical matrices, Born effective charges, dielectric permittivity tensors, and interatomic force constants from density-functional perturbation theory, Phys. Rev. B **55**, 10355 (1997).

[65] P. Giannozzi, S. de Gironcoli, P. Pavone, and S. Baroni, *Ab initio* calculation of phonon dispersions in semiconductors, Phys. Rev. B **43**, 7231 (1991).

[66] Q. Wu, S. Zhang, H.-F. Song, M. Troyer, and A. A. Soluyanov, Wanniertools: An open-source software package for novel topological materials, Comput. Phys. Commun. **224**, 405 (2018).

[67] H. Föppl, E. Busmann, and F.-K. Frorath, Die kristallstrukturen von α-Na_2S_2 und K_2S_2, β-Na_2S_2 und Na_2Se_2, Z. anorg. allg. Chem. **314**, 12 (1962).

[68] P. Böttcher, J. Getzschmann, and R. Keller, Zur kenntnis der dialkalimetalldichalkogenide β-Na_2S_2, K_2S_2, α-Rb_2S_2, β-Rb_2S_2, K_2Se_2, Rb_2Se_2, α-K_2Te_2, β-K_2Te_2 und Rb_2Te_2, Z. Anorg. Allg. Chem. **619**, 476 (1993).

[69] See Supplemental Material at http://link.aps.org/supplemental/10.1103/PhysRevB.108.134310 for detailed structural information of all biatomic alkali-metal sulfides and their phonon dispersion spectra.

[70] Y. Hinuma, G. Pizzi, Y. Kumagai, F. Oba, and I. Tanaka, Band structure diagram paths based on crystallography, Comput. Mater. Sci. **128**, 140 (2017).

[71] J. Li, Q. Xie, J. Liu, R. Li, M. Liu, L. Wang, D. Li, Y. Li, and X.-Q. Chen, Phononic Weyl nodal straight lines in MgB_2, Phys. Rev. B **101**, 024301 (2020).

[72] J. Wang, H. Yuan, M. Kuang, T. Yang, Z.-M. Yu, Z. Zhang, and X. Wang, Coexistence of zero-, one-, and two-dimensional degeneracy in tetragonal SnO_2 phonons, Phys. Rev. B **104**, L041107 (2021).

[73] X. Wang, F. Zhou, T. Yang, M. Kuang, Z.-M. Yu, and G. Zhang, Symmetry-enforced ideal lanternlike phonons in the ternary nitride Li_6WN_4, Phys. Rev. B **104**, L041104 (2021).